

The improved saturation model in nuclei

G.R.Boroun* and B.Rezaei†

Department of Physics , Razi University, Kermanshah 67149, Iran
(Dated: June 3, 2024)

We consider the nuclear shadowing in deep-inelastic scattering corresponding to kinematic regions accessible by future experiments at electron-ion colliders. The gluon distribution at small x is obtained using an improved dipole model depended on the impact parameter for atomic nucleus and compared with nCETQ15 parametrization group. The nuclear shadowing at small x is defined within the color dipole formalism with respect to the mass number A . Its behavior is predicted for light nuclei in a wide range of the impact parameter b and the transverse dipole size r . The nuclear saturation at large- r (small μ^2) is observable. The behavior of the nuclear ratio $\sigma_{\text{dip}}^A/\sigma_0$ is similar to the Golec-Biernat-Wüsthoff (GBW) model in a wide range of r for light and heavy nuclei at small x .

I. Introduction

The structure of hadrons in electron-ion interaction in terms of quarks and gluon distribution functions (PDFs), in deep inelastic scattering (DIS), are interesting in the future circular collider hadron-electron (FCC-he) and the large hadron electron collider (LHeC)[1]. Study of nuclear structure and nuclear collisions will be considered on the electron-Ion collider (EIC) [2,3]. The shadowing effects will be important at small values of the Bjorken variable x which is a consequence of multiple scattering at high energies where a hadron becomes a dense system. Indeed, the QCD dynamics of the saturation effects will be visible at small x . This effect is due to the growth of the gluon density with energy and can be studied in the high-density regime of QCD. Its further growth is expected to slow down due to the non-linear QCD effects associated with the unitarity corrections [4-9]. The saturation scale $Q_s^2(x)$ is characterized on the saturation approach and depends on energy. This marks the transition between the linear and saturation regions.

The nuclear photoabsorption cross sections at small x lie on a single curve when plotted against the variable $Q^2/Q_{s,A}^2$ [10-12], where A is the number of nucleons in a nuclear target with $Q_{s,A}^2 \propto A^j Q_s^2$ where $j \simeq \frac{1}{3}$ or $\frac{4}{9}$ (for large nuclei the value j corresponds to $1/3$) in Refs.[4-6,11-16] and $Q_s^2 \sim x^{-\lambda}$ and $\lambda \simeq 0.3$. Non-linear effects in nuclei are expected when $\alpha_s T_A(b) x g(x) \sim Q^2$ because they have more gluons than protons, where $T_A(b)$ is the nuclear thickness and $g(x)$ is the gluon density¹. The nuclear shadowing at the Bjorken variable $x \ll x_A = \frac{1}{m_N R_A} = 0.15 A^{-1/3}$ becomes important (where R_A is the radius of the target nucleus and m_N is the

nucleon mass [13]).

The behavior of the gluon density at very small x describes the exclusive processes in ep and eA collisions and this is important for connection of the dipole-target amplitude to the integrated gluon density. The gluon recombination, in a fast moving frame, is due to the overlap of the gluon clouds of different nucleons. This makes gluon density in the nucleus with mass number A smaller than A times that in a free nucleon. This behavior is shown in Ref.[17] using the "brute force" method in the momentum space.

The saturation effects at EIC play an important role in the processes $e + A \rightarrow e + X$ in experiments with the variable center-of-mass energy within the range $20 < \sqrt{s} < 140$ GeV. The kinematic regions in experiments at the proposed EIC at the Brookhaven National Laboratory give a deeper knowledge of hadronic structure at high energies [2,3]. This energy is lower than at HERA with $\sqrt{s} = 318$ GeV but the luminosity is higher by a factor of 1000. The EIC will combine the experiences of HERA and RHIC, which will have a strong impact on understanding the small and large- x regions of nuclear shadowing and the EMC effect in comparison with fixed-target kinematics for various nuclei [18-20].

In this paper we consider the nuclear dipole cross sections in the region of small x ($x \leq 0.01$) in the improved dipole picture with respect to the bSat and bCGC models at the kinematical range that will be probed by the EIC and LHeC. The paper is organized as follows. In the next section, we present a brief overview of the formalism needed for the description of the exclusive processes in ep collisions and discuss the distinct models for the dipole-proton scattering amplitude employed in our analysis. In section III, we exhibit the dipole cross section models in eA collisions with respect to the nuclear gluon density. In Section IV a comparison of the results with available data on G^A/A will be shown and the dipole cross sections will be discussed. Finally, in the last section conclusions will be outlined.

*Electronic address: boroun@razi.ac.ir

†Electronic address: brezaei@razi.ac.ir

¹ $G(x, Q^2) = xg(x, Q^2)$ where $G(x, Q^2)$ is the gluon distribution.

II. The Dipole Cross-Section Model for γ^* -p

The scattering between the virtual photon γ^* and the proton is seen as the color dipole. This color dipole picture is a factorization scheme for DIS in electron-proton (ep) and lepton-nucleus (lA) scattering. The dipole cross section is factorized into a light-cone wave function by the following form

$$\sigma_{L,T}^{\gamma^*p}(x, Q^2) = \int dz d^2\mathbf{r} |\Psi_{L,T}(\mathbf{r}, z, Q^2)|^2 \sigma_{\text{dip}}^p(\tilde{x}_f, \mathbf{r}). \quad (1)$$

where the transverse dipole size r and the longitudinal momentum fraction z are defined into the photon momentum [21-26]. Here $\Psi_{L,T}$ are defined by spin averaged light-cone wave functions² of the photon, and $\sigma_{\text{dip}}(\tilde{x}_f, r)$ is the dipole cross-section. The dipole cross-section contains all the information about the target and the strong interaction physics, and it is related to the imaginary part of $(q\bar{q})p$ forward scattering amplitude. The Bjorken variable x is modified by taking into account the active quark mass as it is equivalent to $\tilde{x}_f \equiv x(1 + 4m_f^2/Q^2)$ where m_f is the mass of the quark of flavor f .

The dipole cross section in the eikonal-like approach was proposed³ [27] by

$$\sigma_{\text{dip}}^p(\tilde{x}_f, r) = \sigma_0(1 - e^{-r^2 Q_s^2/4}). \quad (2)$$

The dipole cross section shows the colour transparency property when $r \rightarrow 0$, i.e. $\sigma_{\text{dip}} \sim r^2$, which is pQCD phenomenon and the saturation property at large r , i.e. $\sigma_{\text{dip}} \sim \sigma_0$, which satisfies the unitarity condition. The dipole cross section improved by Bartels-Golec-Biernat-Kowalski (BGBK) [24] with adding the collinear effects⁴. The dipole cross section with implementation of QCD evolution on the gluon distribution reads

$$\sigma_{\text{dip}}^p = \sigma_0 \left\{ 1 - \exp\left(-\frac{\pi^2 r^2 \alpha_s(\mu^2) x g(\tilde{x}_f, \mu^2)}{3\sigma_0}\right) \right\}, \quad (3)$$

where the hard scale μ is assumed to have the form

$$\mu^2 = C/r^2 + \mu_0^2, \quad (4)$$

with the parameters C and μ_0^2 where they are obtained from a fit to the DIS data [24].

By introducing the impact parameter (IP) of the proton, the dipole cross section reads

$$\sigma_{\text{dip}}^p(x, r) = \int d^2b \frac{d\sigma_{\text{dip}}^p}{d^2b} \quad (5)$$

where b is the impact parameter (IP) of the center of the dipole relative to the center of the proton, and

$$\frac{d\sigma_{\text{dip}}^p}{d^2b} = 2(1 - \text{Re } S(b)), \quad (6)$$

where $S(b)$ is the S-matrix element of the elastic scattering, and it is proportional to the dipole area, the strong coupling, the number of gluons in the cloud and the shape function as

$$\frac{d\sigma_{\text{dip}}^p}{d^2b} = 2 \left[1 - \exp\left(-\frac{\pi^2 r^2 \alpha_s(\mu^2) x g(\tilde{x}_f, \mu^2) T(b)}{2N_c}\right) \right]. \quad (7)$$

Here, the function $T(b)$ is determined from a fit to the data by the exponential form

$$T(b) = \frac{1}{2\pi B_G} \exp(-b^2/2B_G), \quad (8)$$

where the parameter B_G was found to be 4.25 GeV⁻² [25].

For multi Pomeron exchange $d\sigma_{\text{dip}}/d^2b = 2N(x, r, b)$, where the eikonalised dipole scattering amplitude can be expanded as

$$N(x, r, b) = \sum_{n=1}^{\infty} \frac{(-1)^{n+1}}{n!} \left[\frac{\pi^2}{2N_c} r^2 \alpha_s(\mu^2) x g(\tilde{x}_f, \mu^2) T(b) \right]^n, \quad (9)$$

where the n -th term in the expansion corresponds to n -Pomeron exchange [25]. In the Color Glass Condensate (CGC) effective theory [28-29] the dipole cross section at small r (i.e., Eq.(8)) reads

$$\frac{d\sigma_{\text{dip}}^p}{d^2b} = \frac{\pi^2 r^2 \alpha_s(\mu^2) x g(\tilde{x}_f, \mu^2) T(b)}{N_c}. \quad (10)$$

The BGBK and CGC models with impact parameters are denoted by the IP-Sat and b-CGC models respectively⁵.

² Where the subscript L and T refer to the transverse and longitudinal polarization state of the exchanged photon.

³ The GBW model was updated in [15] to improve the large Q^2 description of the proton structure function by a modification of the small r behavior of the dipole cross section to include evolution of the gluon distribution.

⁴ Although BGBK model is successful in describing dipole cross section at large values of r as the two models (GBW and BGBK) overlap in this region but they differ in the small r region where the running of the gluon distribution starts to play a significant role. Indeed the improved model of σ_{dip} significantly improves agreement at large values of Q^2 without affecting the physics of saturation responsible for transition to small Q^2 .

⁵ The Balitsky-Kovchegov (BK) equation [30-32] for a dipole scattering amplitude was proposed in terms of the hierarchy of equations for Wilson line operators in the limit of large number of colors N_c . The geometrical scaling (GS) [33] at the high-energy limit of perturbative QCD is obtained from the BK equation [30-32] and the CGC formalism [34]. The BGBK and CGC models considered only the dipole cross section integrated over the impact parameter b [35].

The impact parameter dependence in the b-CGC model of the saturation scale Q_s was introduced [35] by

$$Q_s \equiv Q_s(x, b) = \left(\frac{x_0}{x}\right)^{\lambda/2} \left[\exp\left(-\frac{b^2}{2B_{CGC}}\right) \right]^{1/2\gamma_s}, \quad (11)$$

where the parameter B_{CGC} is a free parameter and is determined by the t distribution of the exclusive diffractive processes at HERA.

III. The Dipole Cross-Section Model for γ^* -A

The saturation scale in γ^* -A interactions, $Q_{s,A}^2$, is defined [8] from the running of the coupling by the following form

$$Q_{s,A}^2 \ln\left(\frac{Q_{s,A}^2}{\Lambda_{QCD}^2}\right) \propto \left(\frac{T_A(b)}{T_A(0)}\right) A^{1/3} Q_s^2 \ln\left(\frac{Q_s^2}{\Lambda_{QCD}^2}\right), \quad (12)$$

where $T_A(b)$ is the nuclear profile function normalized to unity, $\int d^2b T_A(b) = 1$. Here b is the impact parameter (IP) of the center of the dipole relative to the center of the nucleus. In the limit $r \rightarrow 0$, Eq.(12) is rewritten by applying the first scattering approximation in the dipole cross section in the form $Q_{s,A}^2 = \frac{1}{2} A T_A(b) \sigma_0 Q_s^2$. In momentum space, the saturation scale is obtained according to the maximum of the unintegrated gluon distribution by

$$Q_{s,A}^2 \simeq \left[4 \ln\left(\frac{2 A T_A(b) \sigma_0}{2 A T_A(b) \sigma_0 - 1}\right) \right]^{-1} Q_s^2. \quad (13)$$

Here $T_A(b)$ is the nuclear thickness function where is defined in Ref.[36] by

$$T_A(b) = \frac{3R_A}{2\pi r_0^3} \sqrt{1 - \frac{b^2}{R_A^2}}. \quad (14)$$

This is obtained from a hard-sphere model for nuclear distribution in the rest frame

$$\rho_A(r) = \frac{3}{4\pi r_0^3} \theta(R_A - r), \quad (15)$$

as

$$Q_{s,A}^2 \approx Q_s^2 A^{1/3} \sqrt{1 - \frac{b^2}{R_A^2}}, \quad (16)$$

with $r_0 = 1.12$ fm. The nuclear thickness function in the Woods-Saxon distribution by assuming that the positions of the nucleons $\{\mathbf{b}_i\}$ are distributed reads [7]

$$T_A(b) = \int dz \frac{C}{1 + \exp[(\sqrt{b^2 + z^2} - R_A)/d]}. \quad (17)$$

The Woods-Saxon distribution is used for $A > 20$ and for light nuclei ($A < 20$) a gaussian profile is used [37] by the following form

$$T_A(b) = \frac{3}{2\pi R_A^2} \exp(-3b^2/2R_A^2), \quad (18)$$

where the nuclear radius parametrized as $R_A = 0.82A^{1/3} + 0.58$ fm (except deuteron). Therefore the dipole-nucleus cross-section into the positions of the nucleons has been written [7] as

$$\begin{aligned} \frac{d\sigma_{\text{dip}}^A}{d^2b} &= 2 \int \prod_{i=1}^A \{d^2b_i T_A(b_i)\} \left[1 - \prod_{i=1}^A S_p(\mathbf{r}, \mathbf{b} - \mathbf{b}_i; x) \right] \\ &\approx 2 \left[1 - \left(1 - \frac{T_A(\mathbf{b})}{2} \sigma_{\text{dip}}^p \right)^A \right] \\ &\approx 2 \left[1 - \exp(-A T_A(\mathbf{b}) \sigma_{\text{dip}}^p / 2) \right]. \end{aligned} \quad (19)$$

The nuclear γ^* -A interaction is defined as the γ^* -p interaction through

$$\sigma^{\gamma^*A} = \left(\frac{\pi R_A^2}{\pi R_p^2} \right) \sigma^{\gamma^*p}, \quad (20)$$

with

$$Q_{s,A}^2 = \left(\frac{A \pi R_p^2}{\pi R_A^2} \right)^{1/\delta} Q_s^2, \quad (21)$$

where for a nuclear target with the mass number A , the nuclear radius is given by the usual parameterization⁶ $R_A = (1.12A^{1/3} - 0.86A^{-1/3})$ fm, and $\delta = 0.79 \pm 0.02$ [11]. The area of the proton is determined to be $\pi R_p^2 = 1.55 \pm 0.02$ fm² [11].

The nuclear dipole cross section σ_{dip}^A is dependent on the nuclear gluon distribution $g^A(x, Q^2)$ which is defined in Ref.[38] with the replacement $Q_s^2 \rightarrow Q_{s,A}^2$, by the following form⁷

$$\begin{aligned} xg^A(x, Q^2) &= f(A) \frac{3\sigma_0}{4\pi^2 \alpha_s(Q^2)} \left[-Q^2 \exp(-Q^2/Q_{s,A}^2) \right. \\ &\quad \left. + Q_{s,A}^2 (1 - \exp(-Q^2/Q_{s,A}^2)) \right], \end{aligned} \quad (22)$$

where the function $f(A)$ is defined to be $A^{2/3}$ [11] and $Q_{s,A}^2$ is defined to be $Q_{s,A}^2 = A^{1/3} Q_s^2$ [14]⁸. Therefore, the ratio of the color dipole cross section in the nuclear

⁶ This parametrization shows that the growth of the nuclear saturation scale is faster than $A^{1/3}$ for large nuclei.

⁷ The area of the nuclear target is replace by $S^A = A^{2/3} S$, where S is the nucleon target.

⁸ In the improved saturation model, a matching between the dipole model gluon distribution and the collinear approach is given in Ref.[39] using a leading order gluon anomalous dimension γ_{gg} .

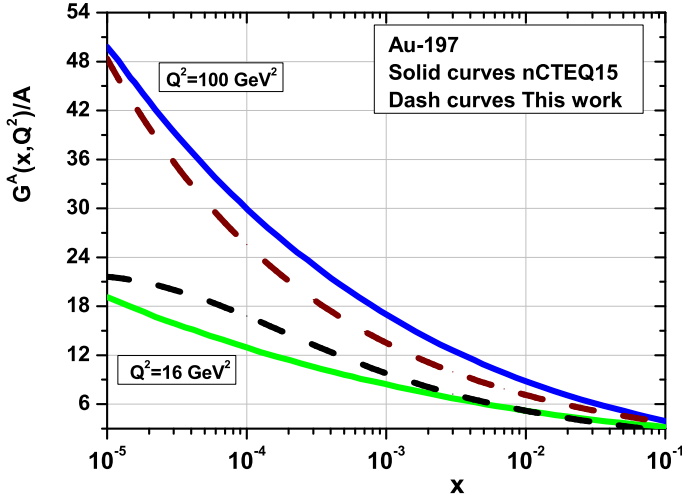


FIG. 1: Results of the nuclear gluon distribution functions for the nucleus of Au – 197. The gluon $G(x, Q^2)$ distributions per nucleon (dash curves) are shown as a function of x for $Q^2 = 16 \text{ GeV}^2$ and $Q^2 = 100 \text{ GeV}^2$, respectively. For comparison, the solid curves show the results of the nCTEQ15 [40] parametrization at the corresponding values of Q^2 , respectively.

improved saturation model, $\sigma_{\text{dip}}^A/\sigma_0$, and at a given impact parameter b are given by

$$\frac{\sigma_{\text{dip}}^A}{\sigma_0} = 1 - \exp\left(-\frac{\pi^2 r^2 \alpha_s(\mu^2) x g^A(\tilde{x}_f, \mu^2)}{3\sigma_0}\right). \quad (23)$$

and

$$\frac{d\sigma_{\text{dip}}^A}{d^2b} = 2 \left[1 - \exp\left(-\frac{\pi^2 r^2 \alpha_s(\mu^2) x g^A(\tilde{x}_f, \mu^2) T_A(b)}{2N_c}\right) \right] \quad (24)$$

IV. Numerical Results

In the leading order running coupling we set $\Lambda_{\text{QCD}} = 120 \text{ MeV}$, which for the one-loop coupling gives $\alpha_s(M_Z^2) = 0.118$ and other parameters are defined by the following forms according to Ref.[16] as

$$\begin{aligned} \sigma_0 &= 29.12 \text{ mb}, \quad \lambda = 0.277, \quad x_0 = 0.41 \times 10^{-4}, \\ m_l &= 0.14 \text{ GeV}, \quad m_c = 1.40 \text{ GeV}. \end{aligned} \quad (25)$$

The results of our numerical studies of the saturation gluon distribution in eA processes, and comparison with the nCTEQ15 [40] for Au – 197 at $Q^2 = 16$ and 100 GeV^2 are shown in Fig.1. In this figure (i.e., Fig.1), we present results of the nuclear gluon distribution function divided by A for the heavy nucleus of Au – 197 as a function of the momentum fraction x .

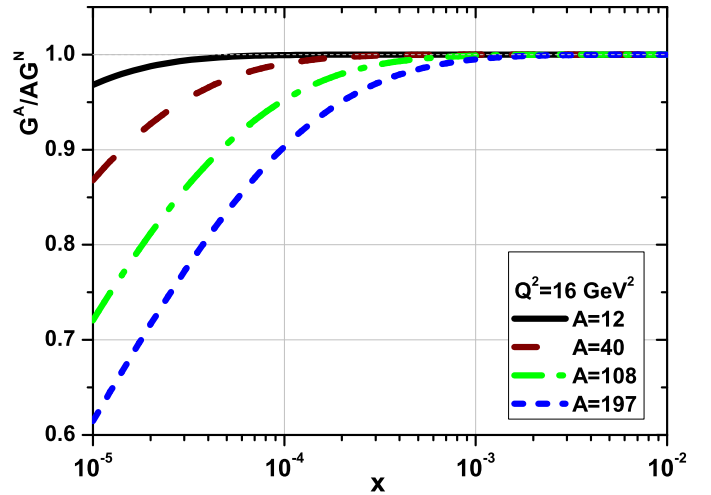


FIG. 2: The ratios $\frac{1}{A} \frac{G^A(x, Q^2)}{G^N(x, Q^2)}$ of gluon distribution functions computed for different values of x for light and heavy nuclei including C-12, Ca-40, Ag-108, Au-197, at $Q^2 = 16 \text{ GeV}^2$.

The dash curves show our results at $Q^2 = 16 \text{ GeV}^2$ and $Q^2 = 100 \text{ GeV}^2$, respectively. They are compared to the nCTEQ15 parametrization at the corresponding values of Q^2 given by the solid curves, respectively. This figure indicates that the results obtained from the present analysis are comparable with the ones obtained from the nCTEQ15 parametrization.

The results for shadowing effects in the gluon distribution of nuclei $\frac{1}{A} \frac{G^A(x, Q^2)}{G^N(x, Q^2)}$ at $Q^2 = 16 \text{ GeV}^2$ for light and heavy nuclei including C-12, Ca-40, Ag-108, Au-197 are shown in Fig.2. We observe that, as expected, the shadowing effects are important for small $x < 10^{-3}$ and their magnitude decreases with a decrease of x and with an increase of the atomic number A [41]. These results are comparable with the results of Ref.[42] of gluon shadowing correction⁹ corresponding to the $|q\bar{q}G >$ Fock component of the photon containing one gluon. These behaviors are observable in other phenomenological parametrizations, such as GBW, KST [43], BGBK and IP-sat models.

In the improved saturation model, the connection between the nuclear dipole cross section, σ_{dip}^A , and the integrated nuclear gluon density is crucial for describe

⁹ In Ref.[42], predictions for the gluon shadowing correction from the $q\bar{q}G$ fluctuation of the photon are shown by the following form $\frac{1}{A} \frac{G^A(x, Q^2)}{G^N(x, Q^2)} \sim 1 - \frac{1}{A} \frac{\Delta\sigma_{\text{tot}}(q\bar{q}G)}{\sigma_{\text{tot}}^{\gamma^*N}(x, Q^2)}$, where $\Delta\sigma_{\text{tot}}(q\bar{q}G)$ is the inelastic correction to the total cross section $\sigma_{\text{tot}}^{\gamma^*N}(x, Q^2)$.

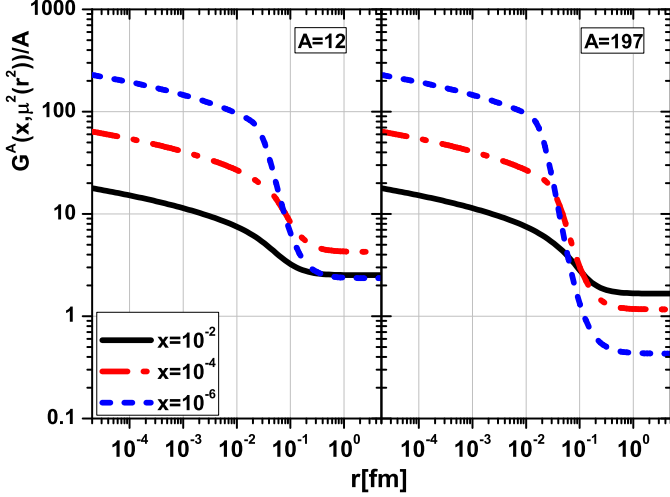


FIG. 3: Results of the nuclear gluon distribution functions for the nucleus of C – 12 and Au – 197. The gluon $G^A(x, \mu^2)$ distributions per nucleon are shown as a function of the dipole transverse size, r , for $x = 10^{-2}$ (solid), $x = 10^{-4}$ (dashed-dot) and $x = 10^{-6}$ (short dashed), respectively.

the exclusive processes in eA collisions [4]. The evolution of the analytical nuclear gluon distribution divided by A for $A=12$ and 197 as a function of the dipole transverse size, r , is shown in Fig.3. In this figure (i.e., Fig.3), we observe a slow decrease of the nuclear gluon distribution in the large dipole domain, for $x = 10^{-2}$ for light and heavy nuclei. This behavior in the large dipole domain is strongly decreases as the Bjorken value decrease and the number of nucleons in a nuclear target increase.

Figure 4 quantifies the size of the dipole cross sections as a function of the mass number A . It presents the ratio $\sigma_{\text{dip}}^A/\sigma_0$ as a function of r for light and heavy nuclei including C-12, Ca-40, Ag-108, Au-197 and the free proton. The ratio for the free proton (short dashed-dot) is compared with the GBW model (short dot-thin, Eq.(2)) in a wide range of r for $x = 10^{-3}$. It is clearly seen where saturation is visible for the free proton at $r \sim 1$ fm and this value decrease as A increases. The improved saturation model in nuclei gives a similar behavior of the ratio $\sigma_{\text{dip}}^A/\sigma_0$ in comparison with the GBW saturation model at low x in a wide range of the dipole transverse size r . Calculations have been performed at the Bjorken variable x to vary in the interval $x = 10^{-6} \dots 10^{-2}$ for Au-197 in Fig.5. The improved saturation model for nuclei gives a good description of the ratio $\sigma_{\text{dip}}^A/\sigma_0$ in comparison with the GBW saturation model at low x in a wide range of the momentum transfer Q^2 . In Fig.5 we observe that, in the interval $2 \cdot 10^{-2} \text{ fm} \lesssim r \lesssim 5 \cdot 10^{-1} \text{ fm}$, a depletion occurs for

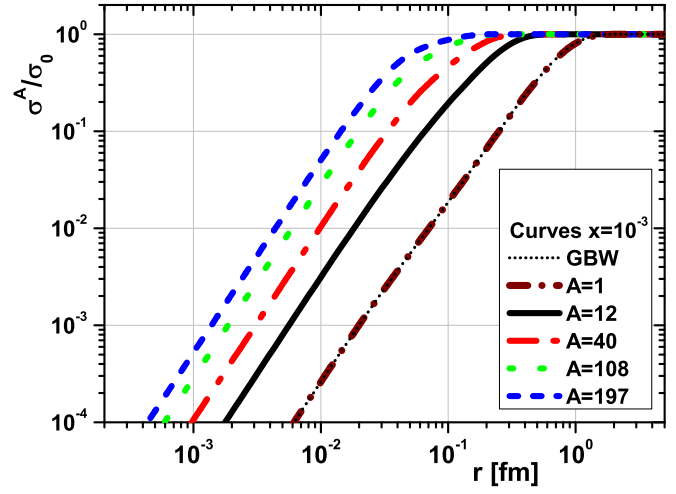


FIG. 4: The ratio $\sigma_{\text{dip}}^A/\sigma_0$ as a function of r at $x = 10^{-3}$ for light and heavy nuclei including C-12 (solid), Ca-40 (dashed-dot), Ag-108 (dot), Au-197 (short-dash) and the free proton (short dashed-dot). The ratio for the free proton (short dashed-dot) is compared with the GBW model (short dot-thin).

$x < 10^{-3}$. This depletion is strongly dependence to the mass number A . In Fig.6 this behavior for the light and heavy nuclei is shown for $x = 10^{-6}$, which significantly enhances the importance of the nonlinear corrections for heavy nuclei compared to the proton case. This effect is visible in the range $1.75 \text{ GeV}^2 < \mu^2 < 3.3 \text{ GeV}^2$ at very low x (i.e., $x = 10^{-6}$) for heavy nuclei. One can see from the figure 6 that the nonlinear effects clearly become more important with increasing A , for small values of x and Q^2 . Indeed, the deviation from unity in this ratio is an indication of color transparency. A depletion in this ratio is called "shadowing", whereas an enhancement is called "anti-shadowing". The anti-shadowing is related to the coherent multiple scattering where it introduces the medium size enhanced (in powers of $A^{1/3}$) nuclear effects [44-49]. The nuclear shadowing is controlled by the interplay of photon lifetime and coherent time fluctuations for transition between no shadowing and saturated shadowing at very small x [50,51].

Depilation and enhancement observed for heavy nuclei in Figs.5 and 6 at very small x at the interval $10^{-2} < r < 10^0$ fm can be dependent on the important of the gluon shadowing from higher $|q\bar{q}G\rangle$ Fock component of the photon in dipole model, which leads

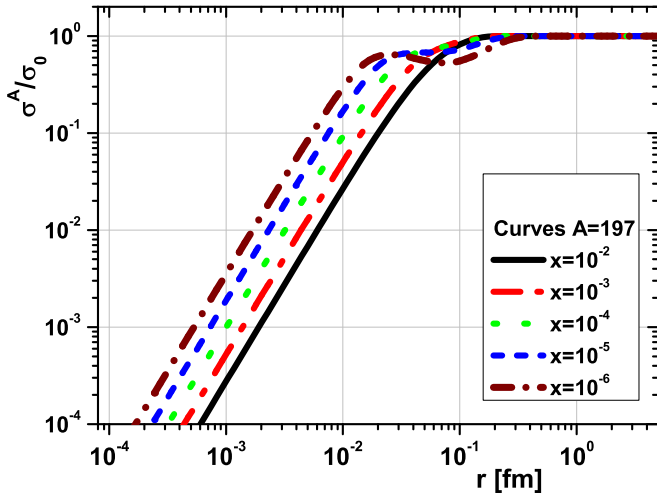


FIG. 5: The extracted ratio $\sigma_{\text{dip}}^A/\sigma_0$ as a function of r at $x = 10^{-6} \dots 10^{-2}$ (curves from left to right, respectively) for Au-197.

to the renormalization of the dipole cross section¹⁰.

In Fig.7, we have plotted the ratio $\sigma_{\text{dip}}^{2A}/\sigma_0^2$ (in the following σ_0^2 and σ^{2A} are suggested to be σ_0^{p+n} and σ_A^{p+n}) for the diffractive¹¹ $q\bar{q}$ production in the color singlet state as a function of r at $x = 10^{-6}$ for light and heavy nuclei including C-12, Ag-108, Pb-208 and the free proton. The diffractive $\gamma^* A \rightarrow q\bar{q} A'$ cross section is proportional to $\sigma_{\text{dip}}^{2A}(x, r)$, where at small values of the diffractive mass $M^2 \sim Q^2$ the elastic scattering of the $q\bar{q}$ pair dominates. In this figure (i.e., Fig.7), we observe that the saddle point increases as the mass number A increases as the magnitude of shadowing is increased using the nuclear density function within the higher Fock component of the photon containing gluons. This behavior of the ratio $\sigma_{\text{dip}}^{2A}/\sigma_0^2$ for heavy nuclei is deeper than the ratio $\sigma_{\text{dip}}^A/\sigma_0$.

In Fig.8, we have added the $q\bar{q}g$ contribution (due to gluon production in the final diffractive state) for the diffractive processes at larger values of the mass $M^2 \gg Q^2$ by a weight factor $C_A/C_F = 2N_C^2/(N_C^2 - 1)$ with $C_A = N_c = 3$ and $C_F = \frac{N_C^2 - 1}{N_C} = \frac{4}{3}$ where N_C is

¹⁰ For further discussion please see Ref.[42].

¹¹ The cross section for the diffractive $q\bar{q}$ production reads

$$\frac{d\sigma_{L,T}^P}{dt}|_{t=0} = \int dz d^2\mathbf{r} |\Psi_{L,T}(\mathbf{r}, z, Q^2)|^2 \sigma_{\text{dip}}^2(\tilde{x}_f, \mathbf{r}),$$

where $t = \Delta^2$, and Δ is the four-momentum transferred into the diffractive system from the proton.

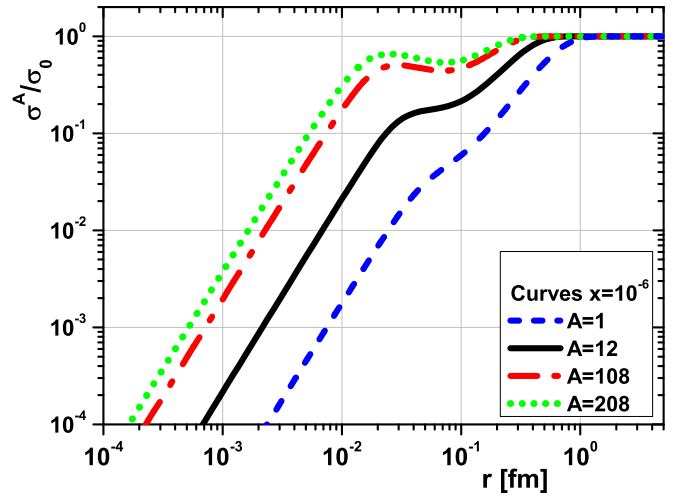


FIG. 6: Results of the nonlinear effects due to the mass number A for the ratio $\sigma_{\text{dip}}^A/\sigma_0$ as a function of r at $x = 10^{-6}$ or a wide range of nuclei including C-12, Ag-108, Pb-208 and the free proton.

the number of colors [17,26-27]. This component was computed in the two gluons exchange approximation with a color octet dipole $\bar{8}8$ where the coupling of two t -channel gluons is relative by the weight factor¹², as the saddle point behavior in the region $10^{-2} < r < 10^0$ fm decreases at $x = 10^{-6}$ for Au-197. This behavior is completely tamed if we consider the propagation of the $|q\bar{q}\rangle >$ Fock component of the photon in a nuclear medium by higher order of shadowing corrections as $|q\bar{q}\rangle > = |q\bar{q}\rangle + |q\bar{q}G\rangle + |q\bar{q}2G\rangle + \dots$ due to different Fock states [42].

In Figs. 9 and 10, we consider the differential cross section $d\sigma_{\text{dip}}^A/d^2b$ at a given impact parameter b , using the definition of the total cross section of the $q\bar{q}$ pair on the proton $\sigma_{q\bar{q}}^p$, by the integrated Woods-Saxon distribution $T_A(b)$ scaled by the number of nucleons, for $x = 10^{-3}$ [38,52]. In these figures (i.e., Figs.9 and 10), the nuclear dipole scatters at impact parameter b are calculated for the nuclei C-12 and Ca-40 in a wide range of the parameters b and r , respectively. We observe that the saturation is visible at $r \approx 1$ fm for C-12 in a wide range of b , $0 \leq b \leq 8$ GeV⁻¹, and

¹² The color dipole cross section for exchange of a two gluon system for octet dipole reads

$$\sigma_{\text{dip}}^p = \sigma_0 \left\{ 1 - \exp\left(-\frac{C_A}{C_F} \frac{\pi^2 r^2 \alpha_s(\mu^2) x g(\tilde{x}_f, \mu^2)}{3\sigma_0}\right) \right\}$$

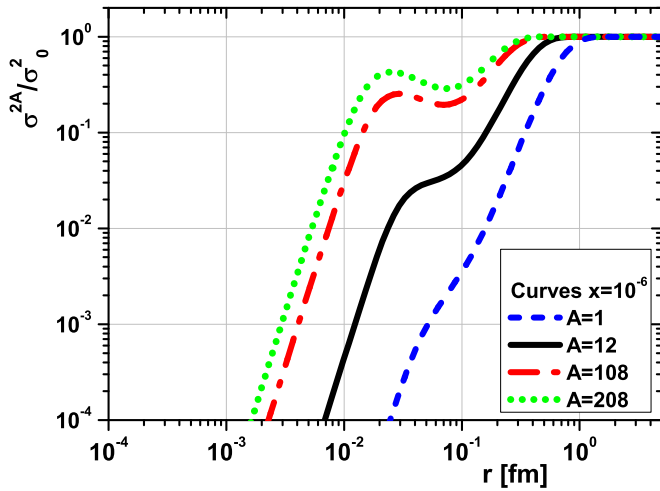


FIG. 7: Results of the nonlinear effects due to the mass number A in the the simplest case of the $q\bar{q}$ system for the ratio $\sigma_{\text{dip}}^{2A}/\sigma_0^2$ as a function of r at $x = 10^{-6}$ for light and heavy nuclei including C-12, Ag-108, Pb-208 and the free proton.

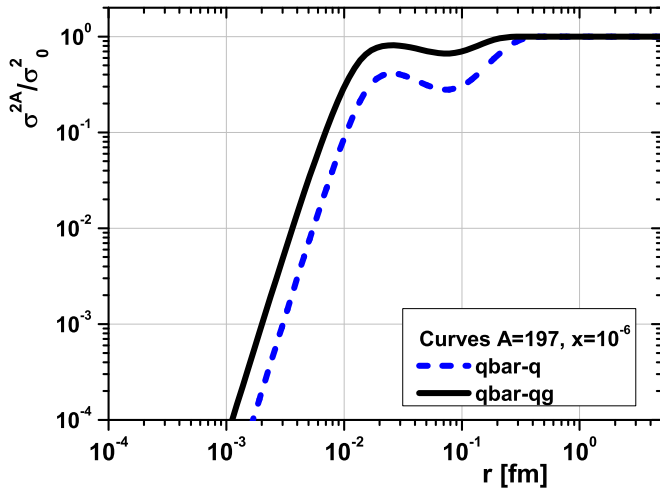


FIG. 8: Comparing between the $q\bar{q}$ and $q\bar{q}g$ components of the diffractive system in the ratio $\sigma_{\text{dip}}^{2A}/\sigma_0^2$ as a function of r at $x = 10^{-6}$ for Au-197.

increase towards lower r (i.e., $r < 1$ fm) when the mass number A increases (see Fig.10 for Ca-40). These 3D figures have a broken line in the behavior of $d\sigma_{\text{dip}}^A/d^2b$ as it increases from approximately $\simeq 0.1$ to 0.5 with an increase A from 12 to 40, respectively. We see that the two functions for C-12 and Ca-40 differ in the small- r

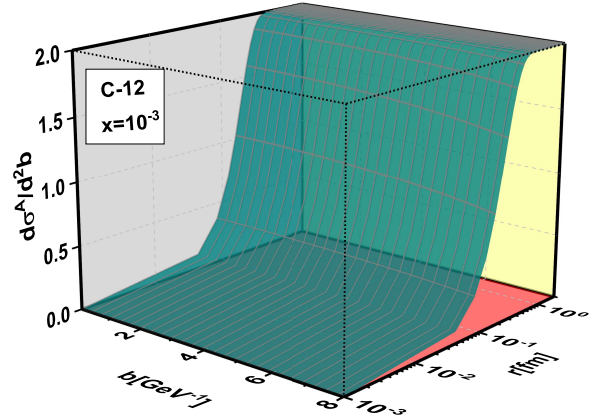


FIG. 9: The nuclear dipole cross section at impact parameter b as a function of r and b at $x = 10^{-3}$ for C-12.

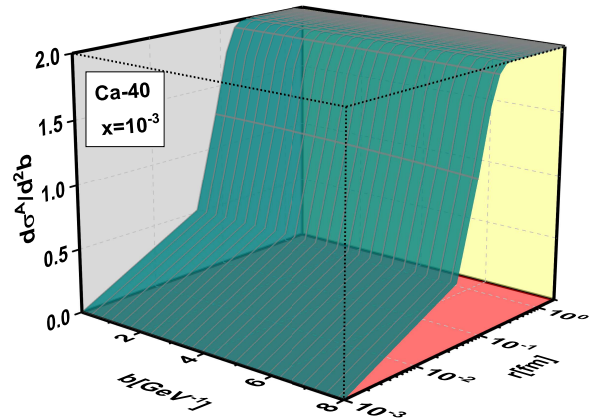


FIG. 10: The same as Fig.9 for Ca-40.

region where the running of the gluon distribution starts to play a significant role, with an increase of the mass number A . Indeed, the behavior of the $d\sigma_{\text{dip}}^A/d^2b$ is directly dependent on the gluon density and the mass number A . These behaviors clearly indicate that the IP saturation model can be used to study nuclear effects in the future experiments at electron-ion colliders.

V. Conclusions

In this paper, we studied the improved saturation model for nuclei with respect to the gluon density obtained within the color dipole approach. The nuclear cross-section is evaluated by implying the impact of the nuclear gluon density at small x . We presented the study of the shadowing in deep-inelastic scattering off nuclei in the kinematic regions accessible by future electron-ion colliders. The dipole cross sections are considered in the description of the inclusive and diffractive DIS at small x in a wide range of the mass number A . The ratio $\sigma_{\text{dip}}^A/\sigma_0$ due to the nuclear effects is similar with the GBW saturation model at low x , although the saturation region expands with the increase of the mass number A . A saddle-shaped behavior is predicted at very low x for heavy nuclei in a range $2 \times 10^{-2} \lesssim r \lesssim 2 \times 10^{-1}$ fm due to the nonlinear effects. In the diffractive DIS processes where the component $q\bar{q}g$ deviates from the GBW and CGC models, the behavior at very low x for heavy nuclei is tamed. This behavior increases the saturation region with the increase of the mass number of A . Nuclear corrections to the impact parameter dependent dipole cross section in a wide range of the impact parameter b and the dipole size r are considered. The saturation region in the IP-Sat model increases as r decreases and the mass number of A increases, in a wide range of b . Indeed, we have tested the IP-Sat model with impact parameter dependence with increases of the mass number of A . While the influence of the impact parameter structure decreases as the mass number of A increases and gives a possibility to test various models for the nuclear dipole cross section at small x at future colliders such as EIC and the LHeC.

ACKNOWLEDGMENTS

The author is grateful to Razi University for the financial support of this project.

REFERENCES

1. LHeC Collaboration and FCC-he Study Group, P. Agostini et al., J. Phys. G: Nucl. Part. Phys. **48**, 110501(2021).
2. A.Accardi et al., Eur.Phys.J.A **52**, 268 (2016).
3. R. Abdul Khalek et al., (2021), arXiv:2103.05419 [physics.ins-det].
4. D.A Fagundes and M.V.T.Machado, Phys.Rev. D **107**, 014004 (2023).
5. V.P.Goncalves and M.V.T.Machado, Eur.Phys.J.C **37**,299 (2004).
6. M.A.Betemps and M.V.T.Machado, arXiv:0906.5593.
7. C.Marquet, Manoel R.Moldes and P.Zurita, Phys.Lett.B **772**, 607 (2017).
8. N.Armesto, Eur.Phys.J.C **26**, 35 (2002).
9. Ya-Ping Xie and Victor P. Goncalves, Phys.Rev. D **105**, 014033 (2022).
10. A. M.Stasto, K.Golec-Biernat and J.Kwiecinski, Phys.Rev.Lett. **86**, 596 (2001).
11. Nestor Armesto, Carlos A. Salgado, Urs Achim Wiedemann, Phys.Rev.Lett. **94**, 022002 (2005).
12. J. Raufeisen, Acta Phys.Polon. B **36**, 235 (2005).
13. N.N.Nikolaev, W.Schafer, B.G.Zakharov and V.R.Zoller, JETP Letters **84**, 537 (2006).
14. F.Carvalho, F.O.Duraes, F.S.Navarra and S.Szpigel, Phys.Rev.C **79**, 035211 (2009).
15. K. Golec-Biernat and S.Sapeta, JHEP **03**, 102 (2018).
16. K.Golec-Biernat, J.Phys.G **28**, 1057 (2002).
17. J.Rausch, V. Guzey and M. Klasen, Phys.Rev.D **107**, 054003 (2023).
18. Y.Hatta, Nucl.Phys.A **00**, 1 (2020).
19. O.Bruning, A. Seryi and S. Verdu-Andres, Front.in Phys. **10**, 886473 (2022).
20. M.Klasen, K.Kovarik and J.Potthoff, Phys. Rev. D **95**, 094013 (2017).
21. J.D.Bjorken, J.B.Kogut and D.E.Sopper, Phys.Rev.D **3**, 1382 (1971).
22. N.N.Nikolaev and B.G.Zakharov, Z.Phys.C **49**, 607 (1991); Z.Phys.C **53**, 331 (1992); Z.Phys.C **64**, 651 (1994); JETP **78**, 598 (1994).
23. A.H.Mueller, Nucl.Phys.B **415**, 373 (1994); A.H.Mueller and B.Patel, Nucl.Phys.B **425**, 471 (1994); A.H.Mueller, Nucl.Phys.B **437**, 107 (1995).
24. J.Bartels, K.Golec-Biernat and H.Kowalski, Phys. Rev. D**66**, 014001 (2002).
25. H.Kowalski and D.Teaney, Phys. Rev. D**68**, 114005 (2003).
26. K.Golec-Biernat, Acta.Phys.Polon.B**33**, 2771 (2002); Acta.Phys.Polon.B**35**, 3103 (2004); J.Bartels, K.Golec-Biernat and H.Kowalski, Acta.Phys.Polon.B**33**, 2853 (2002); E.Iancu, K.Itakura and S.Munier, Phys.Lett.B **590**, 199 (2004); J.R.Forshaw and G.Shaw, JHEP **12**, 052 (2004).
27. K.Golec-Biernat, M.Wüsthoff, Phys.Rev.D **59**, 014017 (1998); Phys.Rev.D **60**, 114023 (1999).
28. A.H. Mueller, Nucl.Phys.B **335**, 115 (1990).
29. L. McLerran and R. Venugopalan, Phys. Rev. D **49**, 2233 (1994).
30. I. Balitsky, Nucl. Phys. B**463**, 99 (1996).
31. Y. V. Kovchegov, Phys. Rev. D**60**, 034008(1999).
32. Y. V. Kovchegov, Phys. Rev. D**61**, 074018 (2000).
33. A.M.Stasto, K.Golec-Biernat and J.Kwiecinski, Phys.Rev.Lett.**86**, 596 (2001).
34. E. Iancu and R. Venugopalan, Quark-Gluon Plasma **3**, (2004) 249, World Scientific Publishing Co Pte Ltd.
35. G.Watt and H.Kowalski, Phys. Rev. D**78**, 014016

- (2008).
36. Yuan-Yuan Zhang and Xin-Nian Wang, Phys.Rev.D **105**, 034015 (2022).
37. A. Capella, A. Kaidalov, C. Merino, D. Pertermann and J. Tran Thanh Van, Eur.Phys.J.C **5**, 111 (1998).
38. R.S.Thorne, Phys.Rev.D **71**, 054024 (2005).
39. R. D. Ball and S. Forte, Phys. Lett. B **335**, 77 (1994).
40. K.Kovarik, A.Kusina, T.Jezo, et al., Phys.Rev.D **93**, 085037 (2016).
41. F.Muhammadi and B.Rezaei, Phys.Rev.C **106**, 025203 (2022).
42. M.Krelina and J.Nemchik, Eur. Phys. J. Plus **135**, 444 (2020).
43. B.Z.Kopeliovich, A.Schafer and A.V.Tarasov, Phys. Rev. D **62**, 054022 (2000).
44. G.R.Boroun, B.Rezaei and S.Heidari, Int.J.Mod.Phys.A **32**, 1750197 (2017).
45. G.R.Boroun and B.Rezaei, Phys.Rev.C **107**, 025209 (2023).
46. S.Heidari, B.Rezaei and G.R.Boroun, Int.J.Mod.Phys.E **26**, 1750067 (2017).
47. E.R.Cazaroto, F.Carvalho, V.P.Goncalves and F.S.Navarra, Phys.Lett.B **669**, 331(2008).
48. X.Guo and J.Li, Nucl. Phys. A **783**, 587 (2007).
49. K. Golec-Biernat et al., Nucl. Phys. B **527**, 289 (1998).
50. G.R.Boroun, Eur.Phys.J.C **82**, 740 (2022).
51. G.R.Boroun, Eur.Phys.J.C **83**, 42 (2023).
52. H.Kowalski and D.Teaney, Phys.Rev.D **68**, 114005 (2003).